REGULAR ARTICLE

blood advances

Gene expression profiling and FDG-PET radiomics uncover radiometabolic signatures associated with outcome in DLBCL

Saveria Mazzara,[1] Laura Travaini,[2] Francesca Botta,[3] Chiara Granata,[4] Giovanna Motta,[1] Federica Melle,[1] Stefano Fiori,[1] Valentina Tabanelli,[1] Anna Vanazzi,[4] Safaa Ramadan,[4,5] Tommaso Radice,[4] Sara Raimondi,[6] Giuliana Lo Presti,[6] Mahila E. Ferrari,[3] Barbara Alicja Jereczek-Fossa,[7,8] Corrado Tarella,[4] Francesco Ceci,[2,8,*] Stefano Pileri,[1,*] and Enrico Derenzini[4,9,*]

[1]Haematopathology Division, European Institute of Oncology (IEO) Istituto di Ricovero e Cura a Carattere Scientifico (IRCCS), Milan, Italy; [2]Nuclear Medicine Division, IEO IRCCS, Milan, Italy; [3]Medical Physics Unit, IEO IRCCS, Milan, Italy; [4]Oncohematology Division, IEO IRCCS, Milan, Italy; [5]NCI-Cairo University, Cairo, Egypt; [6]Molecular and Pharmaco-Epidemiology Unit, Department of Experimental Oncology, IEO IRCCS, Milan, Italy; [7]Division of Radiation Oncology, IEO IRCCS, Milan, Italy; [8]Department of Oncology and Hemato-Oncology, University of Milan, Milan, Italy; and [9]Department of Health Sciences, University of Milan, Milan, Italy

Key Points

- A gene expression signature related to mitochondrial metabolism is associated with specific FDG-PET radiomics profiles and outcome in DLBCL.
- Integration of FDG-PET radiomics with metabolic tumor volume refines PET–based prognostication in DLBCL.

Emerging evidence indicates that chemoresistance is closely related to altered metabolism in cancer. Here, we hypothesized that distinct metabolic gene expression profiling (GEP) signatures might be correlated with outcome and with specific fluorodeoxyglucose positron emission tomography (FDG-PET) radiomic profiles in diffuse large B-cell lymphoma (DLBCL). We retrospectively analyzed a discovery cohort of 48 consecutive patients with DLBCL treated at our center with standard first-line chemoimmunotherapy by performing targeted GEP (T-GEP)– and FDG-PET radiomic analyses on the same target lesions at baseline. T-GEP–based metabolic profiling identified a 6-gene signature independently associated with outcomes in univariate and multivariate analyses. This signature included genes regulating mitochondrial oxidative metabolism (*SCL25A1*, *PDK4*, *PDPR*) that were upregulated and was inversely associated with genes involved in hypoxia and glycolysis (*MAP2K1*, *HIF1A*, *GBE1*) that were downregulated. These data were validated in 2 large publicly available cohorts. By integrating FDG-PET radiomics and T-GEP, we identified a radiometabolic signature (RadSig) including 4 radiomic features (histo kurtosis, histo energy, shape sphericity, and neighboring gray level dependence matrix contrast), significantly associated with the metabolic GEP–based signature (r = 0.43, P = .0027) and with progression-free survival (P = .028). These results were confirmed using different target lesions, an alternative segmentation method, and were validated in an independent cohort of 64 patients. RadSig retained independent prognostic value in relation to the International Prognostic Index score and metabolic tumor volume (MTV). Integration of RadSig and MTV further refined prognostic stratification. This study provides the proof of principle for the use of FDG-PET radiomics as a tool for noninvasive assessment of cancer metabolism and prognostic stratification in DLBCL.

Submitted 25 April 2022; accepted 6 September 2022; prepublished online on *Blood Advances* First Edition 19 September 2022. https://doi.org/10.1182/bloodadvances.2022007825.

*F.C., S.P., and E.D. jointly supervised this study.

Normalized T-GEP and FDG-PET radiomics data can be found in the supplemental tables available with this article.

Raw data are available on request from the corresponding authors, Enrico Derenzini (enrico.derenzini@ieo.it), Stefano Pileri (stefano.pileri@ieo.it), and Francesco Ceci (francesco.ceci@ieo.it).

The full-text version of this article contains a data supplement.

© 2023 by The American Society of Hematology. Licensed under Creative Commons Attribution-NonCommercial-NoDerivatives 4.0 International (CC BY-NC-ND 4.0), permitting only noncommercial, nonderivative use with attribution. All other rights reserved.

Introduction

Metabolic rewiring is a hallmark of cancer and a predominant feature of aggressive lymphoproliferative disorders, such as diffuse large B-cell lymphoma (DLBCL), which need a reshaped metabolism to meet the increased demands related to rapid cell proliferation.[1-4] Emerging evidence indicates that cancer, including lymphoma, is characterized by high metabolic heterogeneity, with diverse metabolic pathways differentially active across cancer types or in the context of specific tumor types.[5,6] In line with this notion, although the occurrence of altered glycolysis in the presence of oxygen, known as the Warburg effect,[7] is one of the main metabolic alterations observed in tumors, some cancer types rely on mitochondrial respiration and oxidative metabolism for survival.[8,9]

Oxidative stress is an unavoidable consequence of oxidative metabolism, playing an important role in cancer progression and chemoresistance.[9-13] In fact, oxidative reprogramming has been mechanistically associated with the development of chemoresistant phenotypes through enhanced nicotinamide adenine phosphate biosynthesis, which counteracts reactive oxygen species generation, allowing cancer cells to survive oxidative stress.[13,14] Despite these notions, the relationship between metabolic rewiring and chemoresistance in lymphoma is poorly defined. DLBCL is a biologically heterogeneous disease as demonstrated by molecular profiling studies, which uncovered distinct DLBCL subsets characterized by specific oncogenic and metabolic dependencies.[15-20] However, despite major advances in the biologic characterization, molecular classifications centered on gene expression profiling (GEP)–based definition of the cell of origin (COO)[15,16] or on *MYC*/*BCL-2* status,[17-19] did not translate yet into tailored therapeutic strategies, because recent precision therapy clinical trials failed to demonstrate significant improvements in outcome compared with standard chemoimmunotherapy.[21-24] Fluorodeoxyglucose positron emission tomography (FDG-PET) is a metabolism-based functional imaging technique, which is considered the standard of care for initial staging and response evaluation in DLBCL.[25] Recently, FDG-PET radiomic analysis gained attention as a noninvasive biologic profiling tool in cancer,[26] and conventional parameters, such as metabolic tumor volume (MTV), are widely accepted prognostic predictors in lymphoma.[27-29] In fact, although FDG-PET uptake is related to glucose metabolism, the application of radiomic analysis to digital FDG-PET images may provide additional information on metabolic rewiring, such as tumor oxygenation status.[30,31]

Furthermore, recent studies have integrated FGD-PET imaging with molecular profiling data to develop more refined patient risk stratification tools in DLBCL.[32,33]

Given these premises, radiomic analysis applied to functional FDG-PET imaging could provide a unique opportunity to explore DLBCL metabolism. In addition, the fact that current first-line chemotherapy regimens are based on oxidative damage–inducing agents makes DLBCL a suitable model to study metabolic determinants of chemoresistance. In this study, we hypothesized that distinct metabolic GEP signatures might be correlated with specific FDG-PET radiomic profiles and outcome following first-line standard chemoimmunotherapy in DLBCL. By integrating targeted GEP (T-GEP) and FDG-PET radiomics, we developed an oxidative metabolism–related GEP signature associated with treatment failure and with a specific FDG-PET radiomic signature, hereafter defined as radiometabolic signature (RadSig), which in turn was found to be an independent outcome predictor. When integrated with MTV, the RadSig further refined prognostic stratification, identifying a subgroup of patients with extremely poor outcome following standard chemoimmunotherapy. These data provide the proof of principle for the use of FDG-PET radiomics as a tool for noninvasive assessment of cancer metabolism and prognostication in DLBCL.

Patients and methods

Study design and patients cohorts

In this retrospective study, we aimed at integrating T-GEP–based metabolic profiling with FDG-PET radiomics to explore the theoretical feasibility of noninvasive metabolic profiling and prognostic stratification in DLBCL. The primary endpoint of this study was the development of an FDG-PET radiomic signature associated with GEP–based metabolic profiling and with progression-free survival (PFS). A 2-phase computational approach was applied, using a discovery cohort for model signature development and an independent validation cohort for model signature validation. We first explored the correlation between GEP–based metabolic profiling and outcome in the discovery cohort performing in silico validation. Then, we assessed the correlation between T-GEP–based metabolic profiling and FDG-PET radiomic signatures and evaluated their prognostic relevance in discovery and validation cohorts. The study design is depicted in Figure 1. Two-hundred thirty consecutive patients with DLBCL with complete clinical and follow-up data were treated with standard R-CHOP (rituximab, doxorubicin, cyclophosphamide, incristine, prednisone)/R-CHOP–like chemoimmunotherapy at IEO, from 2010 to 2018. Baseline FDG-PET performed at IEO was available in 120 cases. Fifty-six patients underwent FDG-PET before the initial diagnostic biopsy, with available FFPE tissue for molecular analyses. Because T-GEP success rate was 85.7% (n = 48), with 8 cases not yielding enough high-quality mRNA to undergo successful GEP assessment, the discovery cohort included 48 consecutive patients. The clinical characteristics of the discovery cohort are shown in Table 1. A second independent cohort including 64 patients treated at our center in the same time frame was used to validate the FDG-PET radiomic signature developed in the discovery cohort (validation cohort). FFPE tissue from initial diagnosis was not available in the validation cohort. Patient characteristics of the validation cohort are summarized in Table 2. In summary, the discovery cohort (n = 48 patients) was profiled with integrated T-GEP and FDG-PET radiomics analyses. Only FDG-PET radiomics data were available in the validation cohort (n = 64 patients).

Two large, independent, publicly available DLBCL cohorts were used for in silico validation of the GEP–based MetSig: a data set from Sha and coworkers (n = 469 patients treated with R-CHOP)[34] with available PFS and overall survival (OS) data, and a data set from Lenz et al (n = 233 patients treated with R-CHOP)[35] with available OS data. Characteristics of patients considered in in silico validation analyses are shown in supplemental Tables 1 and 2.

The study was approved by the institutional review board (protocol number 2863) in accordance with the Declaration of Helsinki.

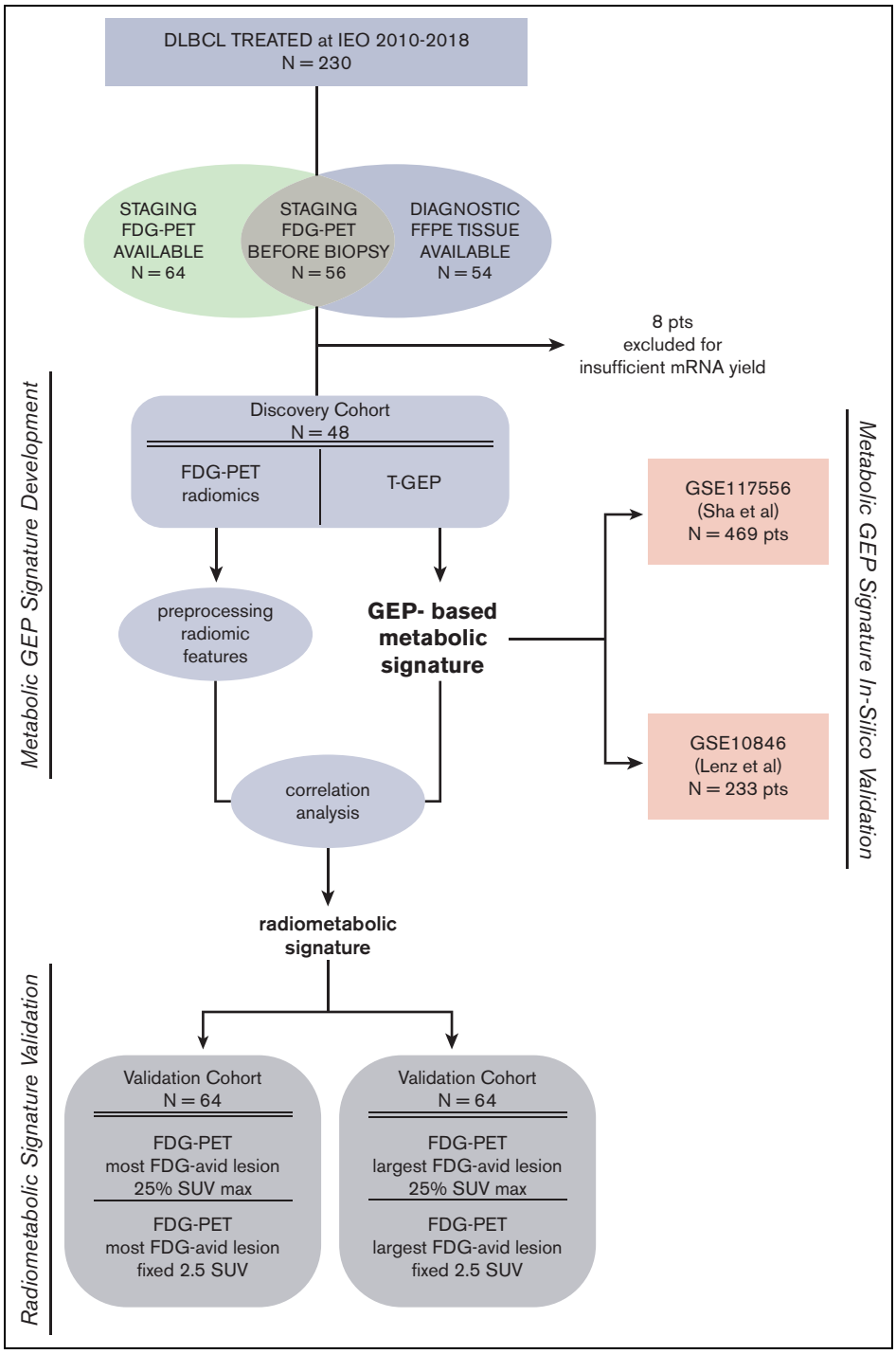

Figure 1. Study design. A total of 230 patients with DLBCL were treated at the IEO, Milan, Italy, from 2010 to 2018. Only patients with available FFPE tissue and baseline FDG-PET scan performed at IEO were initially considered in this analysis. Fifty-six patients had a FDG-PET scan performed before the initial diagnostic biopsy, with available FFPE tissue for molecular analyses. T-GEP success rate was 85.7% (n = 48), with 8 cases not yielding enough high-quality mRNA to undergo successful GEP assessment. Only cases of not otherwise specified (NOS) histology (including those originally diagnosed as DLBCL-NOS and now included in the high-grade B-cell lymphoma provisional category) were considered. Forty-eight patients with NOS-DLBCL with available baseline FDG-PET and mRNA extracted from FFPE tissue samples were finally included in the discovery cohort. A GEP–based metabolic signature (MetSig) was generated in the discovery cohort and validated in silico in 2 large, publicly available DLBCL cohorts (Sha et al and Lenz et al).[34,35] A RadSig was generated in the discovery cohort and validated in an independent series of 64 patients with available baseline FDG-PET scan performed at IEO in the same time frame. FFPE tissue for T-GEP was not available in the validation cohort. IEO, European Institute of Oncology; SUV max, standardized uptake value maximum.

Table 1. Patients' characteristics (discovery cohort)

Variable	Discovery cohort (N = 48 patients)
COO (NanoString), n (%)	
ABC	7 (15)
GCB	33 (69)
UNC	8 (16)
MYC/BCL-2 DEXP mRNA, n (%)	
Yes	10 (21)
No	38 (79)
IPI, n (%)	
Low (0-2)	25 (52)
High (3-5)	23 (48)
Sex, n (%)	
Female	24 (50)
Male	24 (50)
Age, y, median (range)	63 (17-89)
Stage, n (%)	
I	3 (6)
II	10 (21)
III	5 (10)
IV	30 (62)
Follow-up, mo, median (range)	53.97 (2.66-110.85)

ABC, activated B-cell; DEXP, double expressor; GCB, germinal center B-cell; IPI, international prognostic index; UNC, unclassified.

Table 2. Patients' characteristics (validation cohort)

Variable	Validation cohort (N = 64 patients)
COO (NanoString)	
ABC	N/A
GCB	N/A
UNC	N/A
MYC/BCL-2 DEXP mRNA	
Yes	N/A
No	N/A
IPI, n (%)	
Low (0-2)	45 (70)
High (3-5)	19 (30)
Sex, n (%)	
Female	29 (45)
Male	35 (55)
Age, y, median (range)	61.6 (18.1-83.4)
Stage, n (%)	
I	6 (9)
II	20 (31)
III	3 (5)
IV	35 (55)
Follow-up, mo, median (range)	50.26 (0.89-135.48)

N/A, not applicable.

GEP

Digital gene expression quantification was performed in the discovery cohort using the NanoString platform. Total RNA was extracted from 3 sections of 15µm of each FFPE sample using RecoverAll Total Nucleic Acid Isolation Kit for FFPE (Invitrogen). Yield of extracted RNA was assessed using NanoDrop ND 1000 Spectrophotometer (NanoDrop Technologies). RNA quality was scored according to DV200 value (percentage of RNA fragments >200 nucleotides) with the Agilent RNA 6000 Nano Chip Kit (BioAnalyzer, Agilent Technologies); only the samples with a DV200 value >20% passed the quality control step. Gene expression was measured by the NanoString nCounter Analysis System (NanoString Technologies). Two T-GEP panels were used, probing 23 and 180 genes, respectively: 23 genes for COO subtyping and assessment of *MYC*, *BCL-2*, and *NFKBIA* mRNA levels, and 180 target genes involved in metabolic functions. Complete gene lists and normalized $\log_2$ data are available in supplemental Tables 3 and 4. The system computes the relative abundance of each mRNA transcript of interest through a multiplexed hybridization assay and digital readouts of fluorescent-barcoded probes hybridized to each transcript. The nCounter CodeSet containing capture and reporter probes was hybridized to 400 ng of total RNA for 20 hours at 65°C, according to the manufacturer's instructions. Hybridized samples were loaded into the nCounter Prep Station for posthybridization processing. Target mRNA was assessed with nCounter Digital Analyzer. For *MYC*, *BCL-2*, and *NFKBIA* gene expression levels, the definition of high and low values was based on the respective median mRNA levels in the entire cohort.

Image analysis and feature extraction

FDG-PET/computed tomography images were acquired on Discovery ST or Discovery 600 PET/CT scanner (GE Healthcare, Waukesha, WI) with standard procedure according to European guidelines.[36] Quantitative PET image analysis was performed with LifeX package, version 5.1 (INSERM, Alternative Energies and Atomic Energy Commission [CEA], National Centre for Scientific Research [CNRS], Université Paris Sud, Paris, France).[37] First, lesion segmentation was performed by an experienced nuclear medicine physician, identifying all the areas of pathological uptake. The LifeX tool allowed an efficient initial manual segmentation (obtained by inserting "large" spherical regions over the pathological uptake areas), with subsequent refinement automatically applied by the software (thresholding method 1 or 2). More precisely, after manually drawing a region of interest (ROI) totally encompassing each lesion, a SUV threshold was applied within each ROI to identify the lesion boundary. Two different thresholding methods were applied: a percentage threshold equal to 25% of the maximum SUV in the ROI (method 1) and a fixed 2.5 SUV threshold (method 2).[38] MTV was calculated as the sum of all lesions' volumes for each segmentation method. For both segmentation methods, radiomic features were extracted for the following lesions: the lesion investigated with T-GEP analysis (for patients with FFPE tissue available), the lesion with the highest SUV, and the largest FDG-avid lesion.

Before calculation, the 0 to 80 SUV interval was discretized into 256 bins, resulting in a fixed bin size equal to 0.31 SUV. Fifty-five radiomic features were calculated: 3 belonging to the shape category, 15 to the first-order (histogram) category, 37 to the second-order (texture) category. Texture features were obtained from the gray level cooccurrence matrix (calculated twice, considering either 1 or 2 voxels offset), gray level run length matrix, neighboring gray level dependence matrix, and gray level zone length matrix. The full list of extracted features and raw data are reported in supplemental Tables 5 and 6.

Image acquisition modalities and clinical parameters (scanner model, frame duration, injected activity/body weight, time between injection and acquisition, and glucose level), which might have affected image texture and consequently the radiomic features values, were collected for each patient to allow a feature reproducibility analysis (supplemental Table 7).

Development and validation of a RadSig

We first profiled our discovery cohort of 48 patients with available FFPE tissue and baseline PET scans, investigating the association between gene expression levels and PFS. Only genes with $P < .05$ were considered as candidates to develop a predictive metabolic gene signature. We combined the expression levels of significant prognostic genes in a synthetic predictor called MetSig reflective of the balance between protective and risk factors. The prognostic relevance of MetSig was validated in silico in 2 independent publicly available cohorts (GSE117556 and GSE10846).[34,35] Next, we verified the reproducibility and redundancy of radiomic features extracted from baseline FDG-PET images (25% maximum SUV segmentation method) to reduce the risk of false-positive associations. We evaluated feature reproducibility using 4 parameters (scanner, frame, interval, and glycemia levels) using a nonparametric test (analysis of variance or Mann-Whitney test); features with significantly different means according to at least one of the considered parameters were considered not robust and therefore were excluded. Furthermore, a hierarchical clustering analysis of the features' correlation matrix was carried out to identify groups of similar features with high intracluster redundancy and low intercluster correlation,[39] and a Spearman correlation analysis was performed to analyze the correlation between the MetSig and each imaging feature. Radiomic features which were significantly correlated (either positively or negatively) with MetSig were selected ($P < .05$). We tested all possible combinations of these features, applying a stepwise feature selection procedure (detailed in supplemental methods) to generate a synthetic predictor called RadSig characterized by the most significant correlation with the MetSig and PFS.

The prognostic relevance of the RadSig was validated considering different target lesions (the most FGD-avid and the largest lesion) in the discovery cohort and in the validation cohort (n = 64 patients). To increase the sample size for multivariate analyses, a combined analysis of the whole cohort with available FDG-PET data (n = 112, discovery plus validation) was performed. Finally, the robustness of the radiomic signature was evaluated using an alternative segmentation method (the fixed 2.5 SUV threshold).

Statistical analysis

For survival analysis, we used Kaplan-Meier method to estimate OS and PFS.[40] OS was defined as the time between initial diagnosis and death as a result of any cause or last follow-up, whichever occurred first. PFS was defined as the time between initial diagnosis and relapse/progression or death as a result of any cause or last follow-up, whichever occurred first.

A log-rank test assessed significant differences between curves, and the optimum threshold to stratify patients into low-risk and high-risk groups was determined using the maxstat package[41] to yield the smallest log-rank P value. Multivariable and univariate analyses were constructed with the Cox proportional hazards regression model. Associations and differences in patients' characteristics were analyzed with the χ^2 and Fisher exact test. $P \leq .05$ was considered statistically significant. All statistical analyses were performed using R version 3.6.2.[42] Detailed information on gene ontology analyses and receiver operating characteristic (ROC) curve analyses is provided in the supplemental Data.

Results

Development and validation of a metabolic gene expression signature associated with outcome

To investigate the relationship between metabolic rewiring and chemoresistance in DLBCL, we first profiled our discovery cohort (n = 48 patients) with a T-GEP panel (NanoString nCounter 3D Cancer Metabolism panel) including 180 genes belonging to the most relevant cancer metabolism pathways (supplemental Tables 3 and 4). We performed a supervised GEP analysis to identify genes whose expression levels were associated with PFS (supplemental Table 8). Based on these findings, we developed a 6-gene signature, MetSig, which was associated with clinical outcome in univariate and multivariable analyses. The 6-gene MetSig included genes regulating mitochondrial oxidative metabolism and fatty acid oxidation (*SLC25A1*, *PDK4*, *PDPR*), which were upregulated, and was inversely associated with genes involved in hypoxia and glycolytic pathways (*MAP2K1*, *HIF1A*, *GBE1*), which were downregulated (Figure 2A). Notably, as expected, the IPI score was significantly associated with outcome in this cohort (supplemental Figure 1). Although we could not find significant associations between IPI score, COO, *MYC*, and *BCL-2* mRNA levels (high vs low) considered individually (data not shown), we observed a significantly higher proportion of *MYC/BCL-2* mRNA DEXP patients in the MetSig-high compared with the MetSig-low subset (supplemental Table 9). The cellular component of the gene ontology analysis confirmed enrichment in oxidative- and mitochondrial metabolism–related pathways (oxidoreductase complex, TCA cycle, and NADPH oxidase complex) in the MetSig-high subset (Figure 2B). MetSig-high patients had a significantly worse outcome compared with MetSig-low patients in terms of PFS ($P < .0001$) and OS ($P = .0001$) (Figure 2C-D). In multivariable analysis, we found that MetSig status was independently associated with PFS (Figure 2E). Similar results were observed in silico in 2 large, independent, publicly available DLBCL cohorts from Sha et al[34] and Lenz et al[35] (GSE10846 and GSE117556), in which the MetSig consistently retained its significance in univariate and multivariable analyses (Figure 3). Of note, the prognostic value of the COO was confirmed in multivariate analyses in the discovery and Lenz et al[35] cohort, but not in the Sha et al[34] data set (Figure 3B,D). As observed in the discovery cohort, in both validation sets, the proportion of *MYC/BCL-2* DEXP patients was

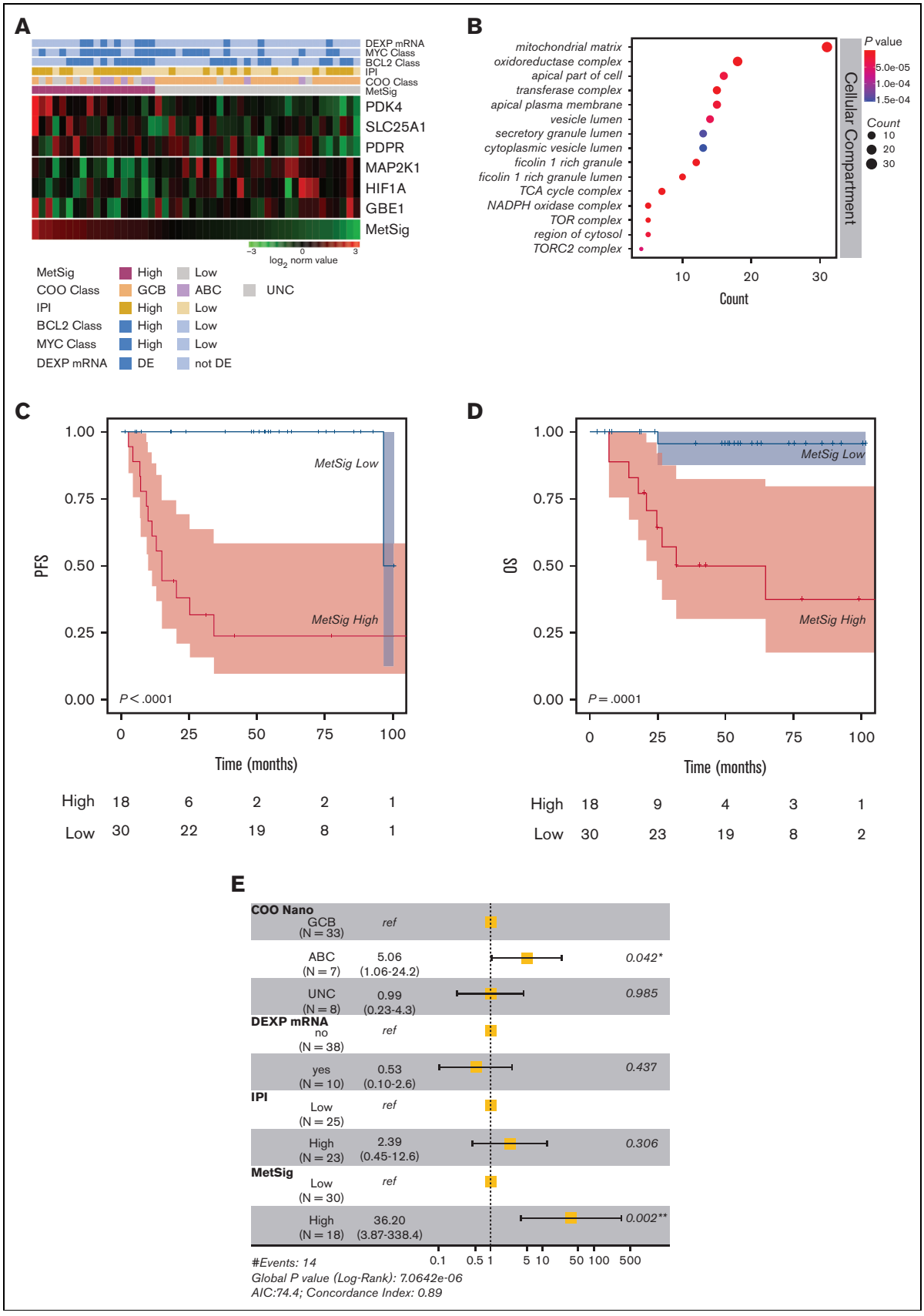
A
DEXP mRNA
MYC Class
BCL2 Class
IPI
COO Class
MetSig
PDK4
SLC25A1
PDPR
MAP2K1
HIF1A
GBE1
MetSig
log2 norm value
MetSig High Low
COO Class GCB ABC UNC
IPI High Low
BCL2 Class High Low
MYC Class High Low
DEXP mRNA DE not DE
B
mitochondrial matrix
oxidoreductase complex
apical part of cell
transferase complex
apical plasma membrane
vesicle lumen
secretory granule lumen
cytoplasmic vesicle lumen
ficolin 1 rich granule
ficolin 1 rich granule lumen
TCA cycle complex
NADPH oxidase complex
TOR complex
region of cytosol
TORC2 complex
Cellular Compartment
P value
5.0e-05
1.0e-04
1.5e-04
Count
10
20
30
Count
C
PFS
MetSig Low
MetSig High
P < .0001
Time (months)
High 18 6 2 2 1
Low 30 22 19 8 1
D
OS
MetSig Low
MetSig High
P = .0001
Time (months)
High 18 9 4 3 1
Low 30 23 19 8 2
E
COO Nano
GCB (N = 33) ref
ABC (N = 7) 5.06 (1.06-24.2) 0.042*
UNC (N = 8) 0.99 (0.23-4.3) 0.985
DEXP mRNA
no (N = 38) ref
yes (N = 10) 0.53 (0.10-2.6) 0.437
IPI
Low (N = 25) ref
High (N = 23) 2.39 (0.45-12.6) 0.306
MetSig
Low (N = 30) ref
High (N = 18) 36.20 (3.87-338.4) 0.002**
#Events: 14
Global P value (Log-Rank): 7.0642e-06
AIC:74.4; Concordance Index: 0.89

Figure 2.

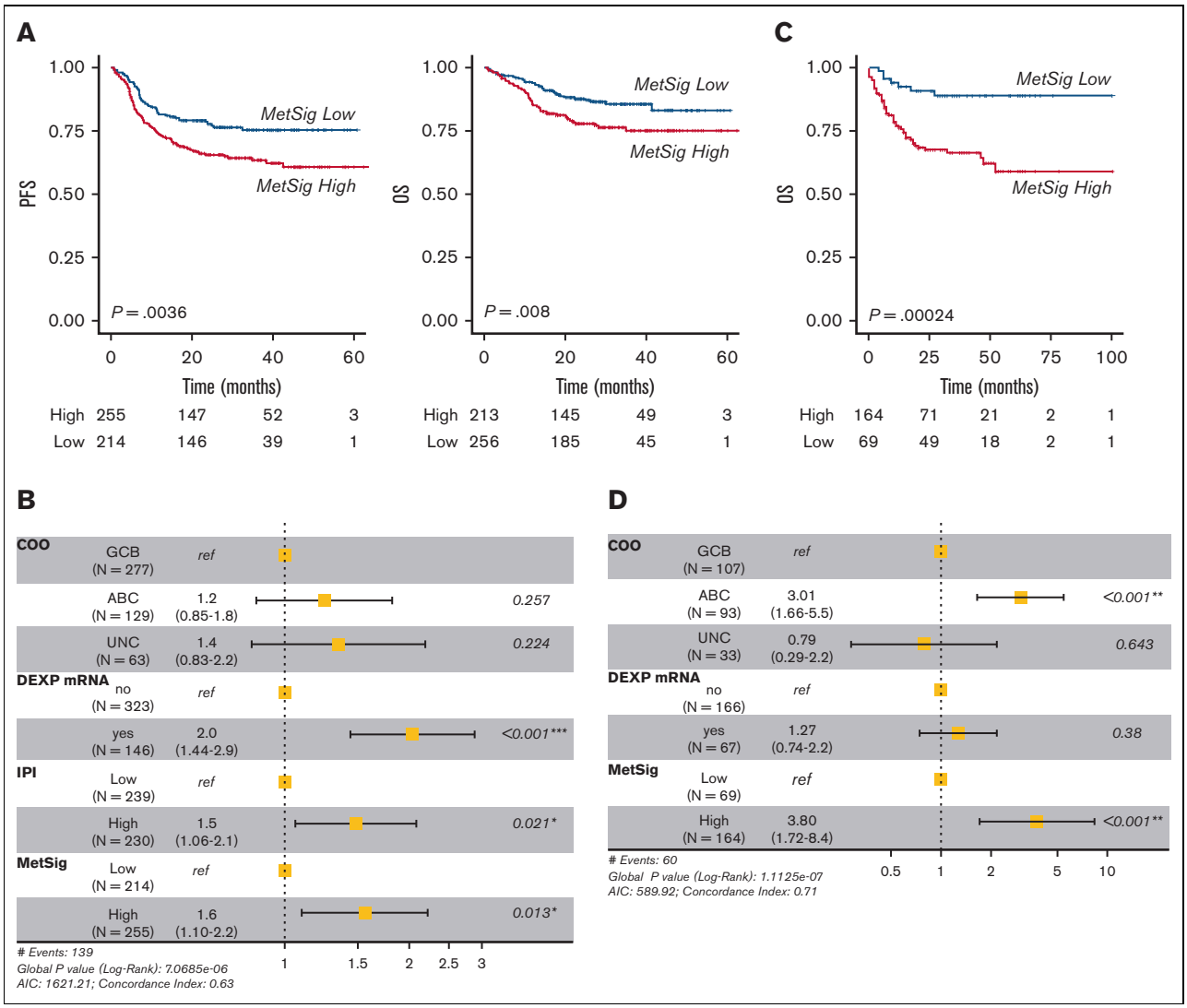

Figure 3. In silico validation of the MetSig. (A) PFS and OS of the 469 patients treated with R-CHOP chemoimmunotherapy in the Sha et al[34] data set according to the T-GEP–based MetSig showing significant differences in outcome between MetSig-low and MetSig-high patients. (B) Forest plot depicting multivariable analyses for PFS in the Sha et al[34] data set. (C) OS of the 233 patients treated with R-CHOP chemoimmunotherapy in the Lenz et al[35] data set according to the MetSig status. (D) Forest plot depicting multivariate analyses for OS (Lenz et al[35] data set).

significantly increased in the MetSig-high subgroups (supplemental Table 9). Focusing the analysis on the Sha et al[34] cohort, no significant differences in the proportion of molecular high-grade or double-hit lymphoma cases were observed between the MetSig-high and MetSig-low subgroups (supplemental Figure 2).

Development of FDG-PET radiomics signature associated with the gene expression–based MetSig

With the aim of investigating the correlation between GEP–based metabolic profiling and specific FDG-PET radiomic signatures, we

Figure 2. A T-GEP–based MetSig related to oxidative metabolism is significantly associated with outcome in DLBCL. (A) Heatmap showing the expression levels of the 6 genes representing the MetSig selected based on supervised PFS analysis. Each row corresponds to 1 Z score normalized gene expression levels and each column corresponds to 1 patient. The expression change from left to right corresponds to the MetSig stratification. (B) Gene ontology analysis showing the cellular component involved in the T-GEP–based metabolic stratification. The node color changes from red to blue in descending order according to the adjusted *P* values. The size of the node represents the number of counts. (C) Kaplan-Meier curve for PFS in patients with DLBCL of the discovery cohort. Patients were divided into 2 groups, MetSig-high vs MetSig-low, by applying the maximally selected rank statistics. MetSig-high patients had significant worse outcome compared with MetSig-low patients. (D) OS of the 48 patients in the discovery cohort according to the MetSig showing significant differences in outcome between MetSig-low and MetSig-high patient subsets. (E) Forest plot depicting multivariable analysis for PFS (discovery cohort). According to this analysis, only the COO as determined by NanoString-based T-GEP (COO Nano) and the MetSig retained statistical significance for PFS. AIC, Akaike information criterion; NADPH, nicotinamide adenine phosphate; ref, reference; TCA, tricarboxylic acid.

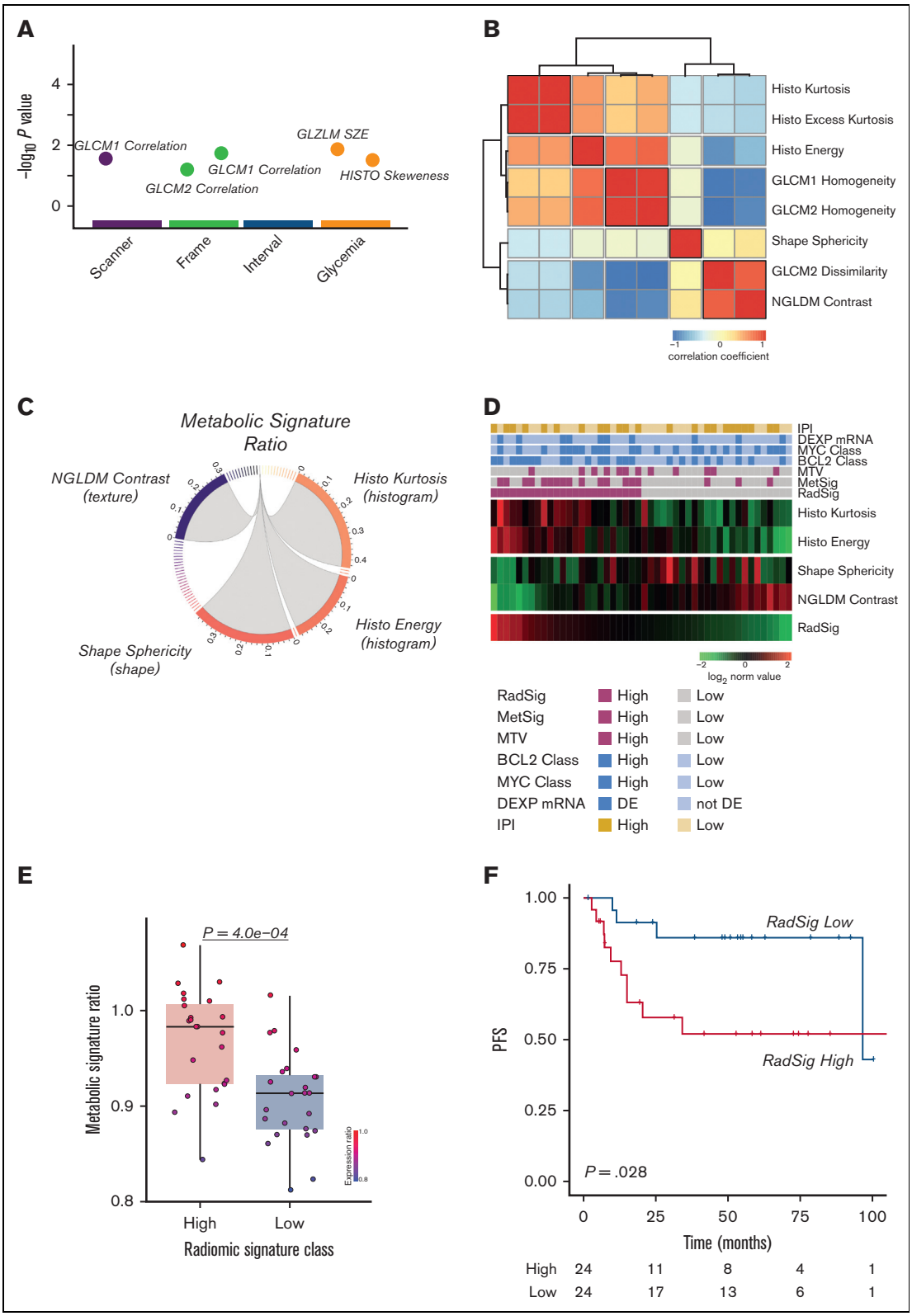

Figure 4. Integration of the T-GEP–based MetSig with FDG-PET radiomics defines a RadSig significantly associated with outcome in DLBCL. (A) Graph illustrating radiomic features considered not robust and excluded because of significantly different values according to scanner model, frame duration, time between injection and acquisition, and glucose level. The x-axis shows the parameters and the corresponding *P* values in negative $\log_{10}$ scale are illustrated on the y-axis. Each circle on the plot represents a single radiomic feature. (B) Correlation matrix heatmap of radiomic features displaying the Spearman correlation coefficient between each pair of radiomic features; radiomic

first extracted PET radiomic features from the same target lesion profiled by T-GEP in the discovery cohort. After semiautomatic segmentation with a 25% SUV maximum threshold, a total of 55 radiomic features were extracted (supplemental Table 5). After reproducibility and redundancy analyses (Figure 4A-B), by applying a stepwise feature selection approach, we identified a radiomic signature including 4 features (histo kurtosis, histo energy, shape sphericity, and NGLDM contrast) (Figure 4C), which was significantly associated with the GEP–based MetSig, and therefore defined as a RadSig (Figure 4D-E). RadSig-high patients had a significantly worse prognosis compared with RadSig-low patients in terms of PFS (Figure 4F). Finally, with the same computational strategy, we tested potential associations between alternative known GEP–based prognostic signatures, such as the COO and the *MYC*, *BCL-2*, and *NFKBIA* signature[43] (MBN-Sig), radiomic features, and outcome. Interestingly, none of the radiomic features found to be correlated with the COO, and the MBN-Sig were significantly associated with outcome. These data confirm the specificity of the observed correlation between MetSig, RadSig, and disease outcome (supplemental Figure 3; supplemental Table 10). The RadSig retained its prognostic significance after adjusting for IPI and MTV in multivariable analysis (supplemental Figure 4A).

Validation of the RadSig

To confirm the robustness of the RadSig, we first tested its prognostic value using different target lesions (ie, the most FDG-avid and the largest FDG-avid lesion) in the discovery cohort of 48 patients. By stratifying patients into RadSig-low and RadSig-high subgroups, the RadSig of the most FGD-avid lesion was a reliable predictor of PFS ($P = .004$) (Figure 5A). These data were confirmed in the validation cohort of 64 patients ($P = .029$) (Figure 5B). To increase the sample size, we performed a combined analysis considering the whole cohort of 112 patients (discovery plus validation), confirming the prognostic value of the RadSig applied to the most FDG-avid lesion ($P = .00032$) (Figure 5C). In the multivariable setting, RadSig retained independent prognostic value for PFS after adjusting for MTV and IPI score (Figure 5D). These observations were confirmed using a different target lesion (the largest FDG-avid lesion) in univariate and multivariable frameworks (Figure 5E-F; supplemental Figure 4B). Finally, the robustness of the RadSig was further validated by using a second segmentation method (fixed 2.5 SUV threshold) (supplemental Figure 5A-D). In addition, ROC curve analysis of RadSig performed on the whole cohort applying the 25% SUV maximum threshold showed an area under the curve (AUC) of 0.96 (95% confidence interval [CI], 0.94-0.99) for both most FDG-avid and largest FDG-avid lesion–based radiomic analyses. Similar performances were obtained using the fixed 2.5 SUV threshold with AUCs of 0.87 (95% CI, 0.82-0.93) and 0.91 (95% CI, 0.86-0.96) using the most FDG-avid lesion and largest FDG-avid lesion, respectively. These results were generated by using a 1000 resampling bootstrap procedure (supplemental methods). Predictive metrics are shown in supplemental Table 11, and ROC curves are displayed in supplemental Figure 6A-D. Overfitting was excluded by introducing a permutation test with 1000 iterations, which confirmed the statistical significance of the AUC value (supplemental Figure 7A-D; supplemental methods).

Integration of MTV and RadSig for prognostic stratification

Because RadSig and MTV were independent prognostic factors in multivariable analyses, we combined these 2 parameters to define a PET–based prognosticator able to further improve patient stratification. By integrating MTV with RadSig status (most FDG-avid lesion) in the whole cohort of 112 patients, we were able to identify a subgroup of patients characterized by high RadSig and high MTV, with an extremely poor outcome in terms of PFS and OS (54% 5-year OS and 26% 5-year PFS) (Figure 6A-B). This FDG-PET–based predictor outperformed the IPI score in multivariable analyses (Figure 6C-D). Similar results were obtained using the largest FDG-avid lesion as the target for the definition of RadSig status and applying an alternative segmentation method (2.5 SUV threshold) (supplemental Figures 8A-D and 9A-D).

Discussion

Here, we investigated the relationship between GEP–based metabolic signatures, FDG-PET radiomic profiles, and outcome in DLBCL. The main aims of this study were (1) to investigate the association between metabolic rewiring and chemoresistance in DLBCL, assessing the correlation between T-GEP–based metabolic profiling, specific FDG-PET radiomic signatures, and PFS and (2) to explore the theoretical feasibility of noninvasive assessment of lymphoma metabolism and prognostic stratification by FDG-PET radiomics.

First, we applied T-GEP to FFPE tissue from the initial diagnosis to develop a GEP–based metabolic signature (MetSig) associated with outcome, and then we integrated T-GEP with FDG-PET radiomic data extracted from the same target lesions to develop a RadSig associated with PFS. This study design implied the availability of enough FFPE tissue for T-GEP and baseline FDG-PET scan performed before the initial diagnostic biopsy. With these stringent criteria, we identified 48 patients who were included in our discovery cohort (Figure 1).

By using a dedicated T-GEP panel including 180 genes involved in cancer metabolism, we first identified a 6-gene MetSig associated with outcome in terms of PFS and OS in the discovery cohort, and we confirmed these findings in silico in 2 large, publicly available validation cohorts (Figures 2 and 3). This signature included

Figure 4 (continued) features were reordered by unsupervised hierarchical clustering for visualizing highly intracorrelated features. Five clusters of radiomic features were generated (the red blocks along the diagonal indicate high intracluster correlation, blue squares indicate negative correlation, and red squares indicate positive correlation). (C) A circos plot showing correlation between the MetSig and radiomic features. Only radiomic features with a significant correlation ($P < .05$) with the MetSig are shown in the circos plot. (D) Heatmap representing the 4 informative radiomic features composing the RadSig shown as rows, and patients with DLBCL samples shown as columns in the discovery cohort. (E) Box plot graph depicting MetSig ratio values in the RadSig-low and -high patient subgroups. *P* value was calculated with the Mann-Whitney Wilcoxon test. (F) PFS of the discovery cohort according to the RadSig status in RadSig-low vs RadSig-high patient subsets. *P* value was calculated with the log-rank test. GLCM, gray level coorcuurence matrix; NGLDM, neighboring gray level dependence matrix.

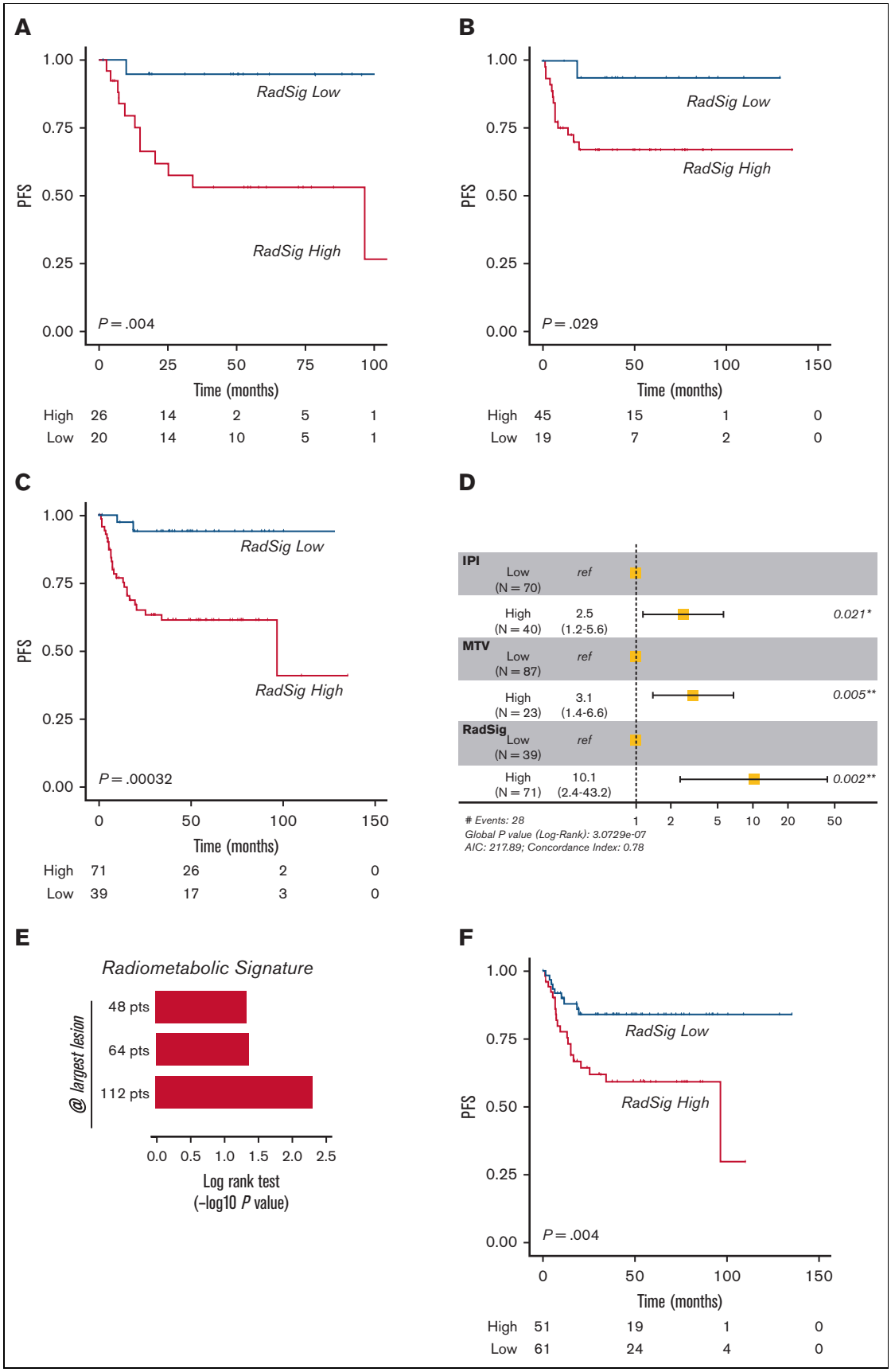
A
1.00
0.75
0.50
0.25
0.00
PFS
RadSig Low
RadSig High
P = .004
0
25
50
75
100
Time (months)
High 26 14 2 5 1
Low 20 14 10 5 1
B
1.00
0.75
0.50
0.25
0.00
PFS
RadSig Low
RadSig High
P = .029
0
50
100
150
Time (months)
High 45 15 1 0
Low 19 7 2 0
C
1.00
0.75
0.50
0.25
0.00
PFS
RadSig Low
RadSig High
P = .00032
0
50
100
150
Time (months)
High 71 26 2 0
Low 39 17 3 0
D
IPI
Low (N = 70) ref
High (N = 40) 2.5 (1.2-5.6) 0.021*
MTV
Low (N = 87) ref
High (N = 23) 3.1 (1.4-6.6) 0.005**
RadSig
Low (N = 39) ref
High (N = 71) 10.1 (2.4-43.2) 0.002**
Events: 28
Global P value (Log-Rank): 3.0729e-07
AIC: 217.89; Concordance Index: 0.78
1
2
5
10
20
50
E
Radiometabolic Signature
@ largest lesion
48 pts
64 pts
112 pts
0.0
0.5
1.0
1.5
2.0
2.5
Log rank test
(−log10 P value)
F
1.00
0.75
0.50
0.25
0.00
PFS
RadSig Low
RadSig High
P = .004
0
50
100
150
Time (months)
High 51 19 1 0
Low 61 24 4 0

Figure 5.

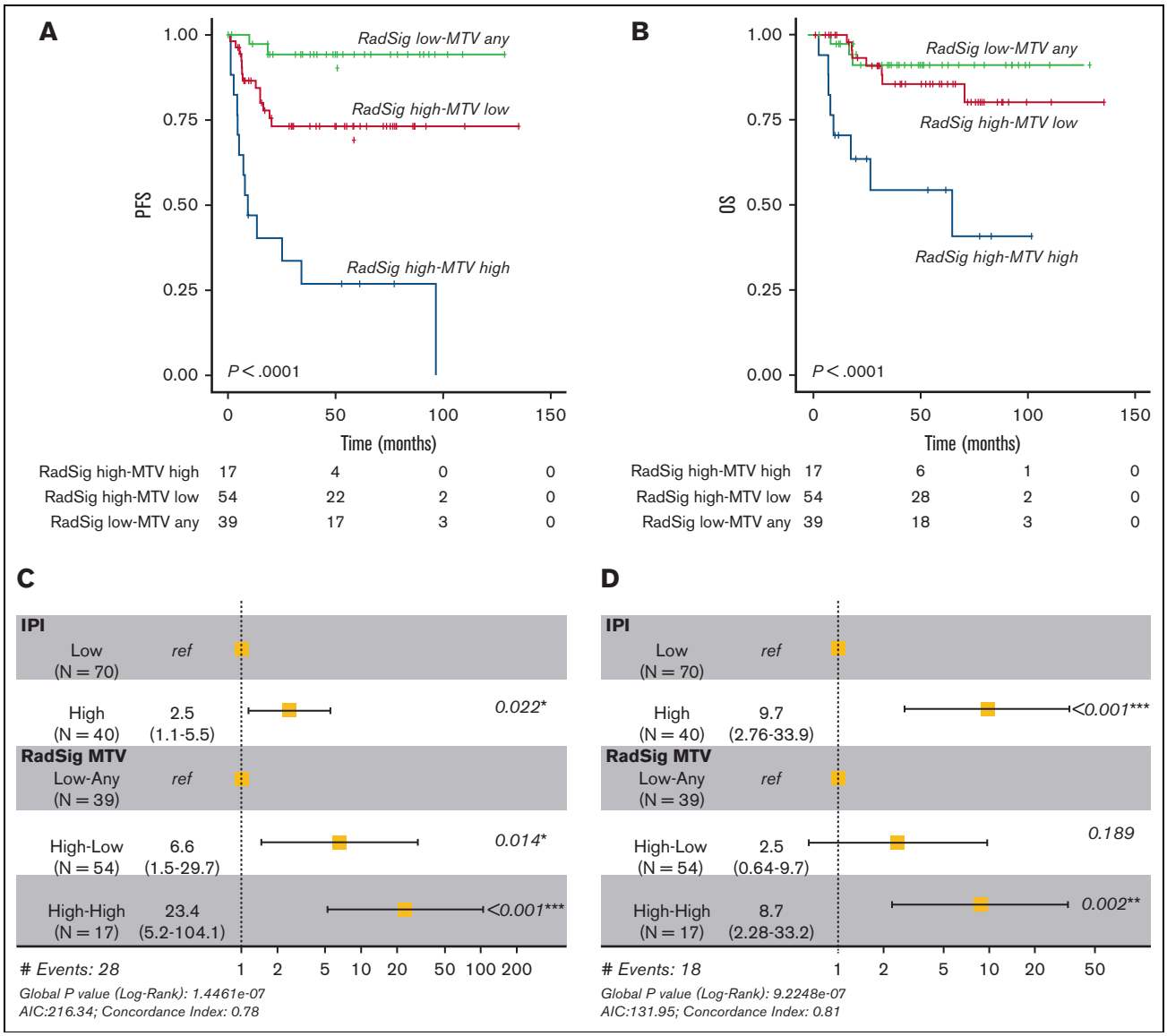

Figure 6. Integration of RadSig and MTV refines risk stratification in DLBCL. (A) PFS of the whole cohort of 112 patients according to the combination of MTV and RadSig status (integrated RadSig-MTV model). *P* value was calculated with the log-rank test. (B) OS in the whole cohort (112 patients) according to the integrated RadSig-MTV model. (C,D) Forest plots depicting multivariable analyses confirming a significant independent association with PFS and OS of the integrated RadSig-MTV model in the whole cohort after controlling for the IPI.

upregulated genes related to mitochondrial oxidative metabolism, such as *PDK4*, *SCL25A1*, and *PDPR*, and was inversely associated with genes involved in hypoxia and glycolysis, such as *MAP2K1*, *HIF1A*, and *GBE1*. Then, we identified a 4-feature RadSig correlated with the GEP–based MetSig and clinical outcome in terms of PFS (Figure 4). Importantly, the specificity of the observed association between MetSig, RadSig, and outcome was confirmed by testing alternative GEP–based signatures, such as the COO and the MBN-Sig,[43] which did not allow the identification of outcome-associated radiomic predictors. The robustness of this RadSig was validated in an independent cohort of 64 patients with available baseline FDG-PET scans treated at our center during the same period, using different target lesions (most FDG-avid and largest FDG-avid lesion) and different segmentation

Figure 5. RadSig validation. (A) Kaplan-Meier curve of PFS according to the RadSig status, as calculated by using a different target lesion, that is, the most FDG-avid lesion. (B) PFS of the independent validation cohort of 64 patients, according to RadSig status (most FDG-avid lesion). (C) PFS of the whole cohort of 112 patients (discovery and validation), according to the RadSig status (most FDG-avid lesion). (D) Forest plot depicting multivariable analyses performed in the whole cohort of 112 patients. (E) Bar plot depicting the RadSig performance using a different target lesion (largest FDG-avid lesion) in the considered patients' subsets (discovery cohort of 48 patients, validation cohort of 64 patients, and combined cohort of 112 patients). (F) PFS according to RadSig status (largest FDG-avid lesion) in the whole cohort of 112 patients.

methods (25% SUV maximum and 2.5 SUV threshold) (Figure 5). Furthermore, internal validation methods (bootstrap correction and permutation model) confirmed the performance of RadSig. Notably, in multivariable analyses, the RadSig was an independent prognostic predictor with respect to known clinical prognosticators (IPI score) and conventional parameters, such as MTV. Following these observations and because MTV is a widely accepted prognostic predictor in DLBCL,[26-28] we integrated RadSig with MTV to refine our PET–based prognosticator. The integration of RadSig and MTV identified a patient's subset (RadSig-high-MTV-high) with a dismal outcome (54% 5-year OS and 26% 5-year PFS) (Figure 6). The robustness of these findings was confirmed using different target lesions to define RadSig status and applying different segmentation methods. These data indicate that baseline FDG-PET radiomics has the potential to identify upfront those patients with dismal outcome following standard chemoimmunotherapy and thus, are potentially eligible for alternative treatment strategies.

Here, we demonstrate that a GEP-based signature related to mitochondrial oxidative metabolism is associated with a poor outcome following standard anthracycline-based chemoimmunotherapy in DLBCL. These findings could suggest a functional switch from glycolysis to oxidative metabolism in chemoresistant DLBCL, in line with similar observations performed in different tumor models.[44-46] In particular, upregulation of *PDK4* and *SLC25A1* has been associated with chemoresistance and radioresistance in multiple cancer types.[47-50]

It is noteworthy that anthracyclines induce oxidative stress and DNA damage through increased reactive oxygen species generation,[51] and in line with this, resistance to doxorubicin has been associated with cell-intrinsic mechanisms counteracting oxidative stress induction in poor prognosis DLBCL subsets, such as ABC–derived DLBCL.[52] Furthermore, we recently demonstrated that overexpression of oxidative and replicative stress biomarkers defines a *MYC/BCL-2*–positive DLBCL subpopulation enriched in ABC and double-hit lymphoma characterized by a dismal outcome following anthracycline-based chemotherapy.[53] Interestingly, we observed a significant enrichment of *MYC/BCL-2* mRNA DEXP DLBCL in the MetSig-high subset, confirming the presence of oxidative metabolic rewiring in a significant proportion of *MYC/BCL-2*–positive DLBCLs. Finally, recent data indicate that *MYC*-driven DLBCLs rely on oxidative metabolism being exquisitely sensitive to targeted inhibition of the mitochondrial respiratory chain in preclinical models.[54] These data are in line with the notion that oxidative metabolic rewiring could be a powerful and unifying determinant of poor prognosis in DLBCL, supporting the development of treatment strategies based on pharmacologic disturbance of mitochondrial metabolism and antioxidant response to overcome chemoresistance. In this light, it is worth noting that the metabolic GEP signature identified in this study could be potentially druggable because small-molecule inhibitors of PDK4 and SLC25A1 are currently in preclinical development.[47,55]

This study has some intrinsic limitations, which may restrain the generalizability of the results, such as the single-institution nature and the small sample size of discovery and validation sets. However, although PET image segmentation was performed by a single operator, the use of thresholding methods could mitigate reproducibility issues, and additional analyses such as bootstrapping were used to confirm the robustness of the RadSig. In any case, given the aforementioned limitations, these results need to be validated in prospective studies.

In conclusion, this study represents a proof of concept for the use of FDG-PET radiomics as a tool for noninvasive assessment of cancer metabolic rewiring, providing the rationale for the development of therapeutic strategies aimed at targeting mitochondrial metabolism in DLBCL.

Acknowledgments

The authors thank Laura Carpen and Alessandro Raveane for bioinformatic support and Maria Rosaria Sapienza for helpful discussions on biological topics.

This study was funded by the AIRC 5 × 1000 grant (number 21198) (S.P.), the Italian Ministry of Health for Institutional Research (Ricerca Corrente), and a research grant from the Italian Ministry of Health (grant GR-2016 to 02362050) (G.L.P.).

Authorship

Contribution: E.D., S.P., F.C., and S.M. conceived the study, analyzed the data, and wrote the manuscript; F.M. and G.M. performed targeted gene expression profiling; C.T., L.T., F.B., C.G., S.F., V.T., A.V., S. Ramadan, T.R., S. Raimondi, G.L.P., M.E.F., B.A.J-F., and F.C. analyzed the data and critically reviewed the manuscript; and all authors critically reviewed the manuscript and approved the final version of the manuscript.

Conflict-of-interest disclosure: C.T. is a member of the advisory board for ADC Therapeutics and AbbVie. S.P. is a member of the advisory board for Celgene, NanoString, Roche, and BeiGene. E.D. received research funding from TG Therapeutics, ADC Therapeutics, and Takeda and is a member of the advisory board for BeiGene, AstraZeneca, AbbVie, and Roche. F.C. is a member of the advisory board for Novartis and reports personal fees and consultant honoraria from Bayer, Janssen Oncology, and Novartis Advanced Accelerator Applications, outside of the present study. The remaining authors declare no competing financial interests.

ORCID profiles: G.M., 0000-0001-5593-5397; V.T., 0000-0002-4142-2248; A.V., 0000-0002-2977-4208; S.R., 0000-0003-4673-9049; G.L.P., 0000-0003-4023-2589; M.E.F., 0000-0002-4373-8588; F.C., 0000-0001-9785-5248; S.P., 0000-0001-8032-5128; E.D., 0000-0002-7154-8140.

Correspondence: Enrico Derenzini, Oncohematology, European Institute of Oncology (IEO) Istituto di Ricovero e Cura a Carattere Scientifico (IRCCS), Via Ripamonti 435, 20141 Milan, Italy; email: enrico.derenzini@ieo.it; Stefano Pileri, Haematopathology Division, IEO IRCCS, Via Ripamonti 435, 20141 Milan, Italy; email: stefano.pileri@ieo.it; and Francesco Ceci, Nuclear Medicine Division, IEO IRCCS, Via Ripamonti 435, 20141 Milan, Italy; email: francesco.ceci@ieo.it.

References

1. DeBerardinis RJ, Lum JJ, Hatzivassiliou G, Thompson CB. The biology of cancer: metabolic reprogramming fuels cell growth and proliferation. *Cell Metabol*. 2008;7(1):11-20.
2. Tennant DA, Durán RV, Gottlieb E. Targeting metabolic transformation for cancer therapy. *Nat Rev Cancer*. 2010;10(4):267-277.
3. Ricci JE, Chiche J. Metabolic reprogramming of non-Hodgkin's B-cell lymphomas and potential therapeutic strategies. *Front Oncol*. 2018;8:556.
4. Eberlin LS, Gabay M, Fan AC, et al. Alteration of the lipid profile in lymphomas induced by MYC overexpression. *Proc Natl Acad Sci USA*. 2014;111 (29):10450-10455.
5. Kim J, DeBerardinis RJ. Mechanisms and implications of metabolic heterogeneity in cancer. *Cell Metabol*. 2019;30(3):434-446.
6. Strickaert A, Saiselet M, Dom G, et al. Cancer heterogeneity is not compatible with one unique cancer cell metabolic map. *Oncogene*. 2017;36(19): 2637-2642.
7. Warburg O, Wind F, Negelein E. The metabolism of tumors in the body. *J Gen Physiol*. 1927;8(6):519-530.
8. Courtnay R, Ngo DC, Malik N, Ververis K, Tortorella SM, Karagiannis TC. Cancer metabolism and the Warburg effect: the role of HIF-1 and PI3K. *Mol Biol Rep*. 2015;42(4):841-851.
9. Guerra F, Arbini AA, Moro L. Mitochondria and cancer chemoresistance. *Biochim Biophys Acta Bioenerg*. 2017;1858(8):686-699.
10. Hayes JD, Dinkova-Kostova AT, Tew KD. Oxidative stress in cancer. *Cancer Cell*. 2020;38(2):167-197.
11. Kuehne A, Emmert H, Soehle J, et al. Acute activation of oxidative pentose phosphate pathway as first-line response to oxidative stress in human skin cells. *Mol Cell*. 2015;59(3):359-371.
12. Purohit V, Simeone DM, Lyssiotis CA. Metabolic regulation of redox balance in cancer. *Cancers*. 2019;11(7):955, 1-24.
13. Germain N, Dhayer M, Boileau M, Fovez Q, Kluza J, Marchetti P. Lipid metabolism and resistance to anticancer treatment. *Biology*. 2020;9(12):474, 1-21.
14. Evans KW, Yuca E, Scott SS, et al. Oxidative phosphorylation is a metabolic vulnerability in chemotherapy-resistant triple-negative breast cancer. *Cancer Res*. 2021;81(21):5572-5581.
15. Alizadeh AA, Eisen MB, Davis RE, et al. Distinct types of diffuse large B-cell lymphoma identified by gene expression profiling. *Nature*. 2000;403(6769): 503-511.
16. Shipp MA, Ross KN, Tamayo P, et al. Diffuse large B-cell lymphoma outcome prediction by gene-expression profiling and supervised machine learning. *Nat Med*. 2002;8(1):68-74.
17. Hu S, Xu-Monette ZY, Tzankov A, et al. MYC/BCL2 protein coexpression contributes to the inferior survival of activated B-cell subtype of diffuse large B-cell lymphoma and demonstrates high-risk gene expression signatures: a report from The International DLBCL Rituximab-CHOP Consortium Program. *Blood*. 2013;121(20):4021-4031.
18. Green TM, Young KH, Visco C, et al. Immunohistochemical double-hit score is a strong predictor of outcome in patients with diffuse large B-cell lymphoma treated with rituximab plus cyclophosphamide, doxorubicin, vincristine, and prednisone. *J Clin Oncol*. 2012;30(28):3460-3467.
19. Johnson NA, Slack GW, Savage KJ, et al. Concurrent expression of MYC and BCL2 in diffuse large B-cell lymphoma treated with rituximab plus cyclophosphamide, doxorubicin, vincristine, and prednisone. *J Clin Oncol*. 2012;30(28):3452-3459.
20. Caro P, Kishan AU, Norberg E, et al. Metabolic signatures uncover distinct targets in molecular subsets of diffuse large B cell lymphoma. *Cancer Cell*. 2012;22(4):547-560.
21. Younes A, Sehn LH, Johnson P, et al. Randomized phase III trial of ibrutinib and rituximab plus cyclophosphamide, doxorubicin, vincristine, and prednisone in non-germinal center B-cell diffuse large B-cell lymphoma. *J Clin Oncol*. 2019;37(15):1285-1295.
22. Nowakowski GS, Chiappella A, Gascoyne RD, et al. ROBUST: a phase III study of lenalidomide plus R-CHOP versus placebo plus R-CHOP in previously untreated patients with ABC-type diffuse large B-cell lymphoma. *J Clin Oncol*. 2021;39(12):1317-1328.
23. Davies A, Cummin TE, Barrans S, et al. Gene-expression profiling of bortezomib added to standard chemoimmunotherapy for diffuse large B-cell lymphoma (REMoDL-B): an open-label, randomized, phase 3 trial. *Lancet Oncol*. 2019;20(5):649-662.
24. Morschhauser F, Feugier P, Flinn IW, et al. A phase 2 study of venetoclax plus R-CHOP as first-line treatment for patients with diffuse large B-cell lymphoma. *Blood*. 2021;137(5):600-609.
25. Cheson BD, Fisher RI, Barrington SF, et al. Recommendations for initial evaluation, staging, and response assessment of Hodgkin and non-Hodgkin lymphoma: the Lugano classification. *J Clin Oncol*. 2014;32(27):3059-3068.
26. Cottereau AS, Lanic H, Mareschal S, et al. Molecular profile and FDG-PET/CT total metabolic tumor volume improve risk classification at diagnosis for patients with diffuse large B-cell lymphoma. *Clin Cancer Res*. 2016;22(15):3801-3809.
27. Vercellino L, Cottereau AS, Casasnovas O, et al. High total metabolic tumor volume at baseline predicts survival independent of response to therapy. *Blood*. 2020;135(16):1396-1405.
28. Kostakoglu L, Mattiello F, Martelli M, et al. Total metabolic tumor volume as a survival predictor for patients with diffuse large B-cell lymphoma in the GOYA study. *Haematologica*. 2022;107(7):1633-1642.

29. Cook GJR, Azad G, Owczarczyk K, Siddique M, Goh V. Challenges and promises of PET radiomics. *Int J Radiat Oncol Biol Phys*. 2018;102(4):1083-1089.

30. Yamamoto K, Brender JR, Seki T, et al. Molecular imaging of the tumor microenvironment reveals the relationship between tumor oxygenation, glucose uptake, and glycolysis in pancreatic ductal adenocarcinoma. *Cancer Res*. 2020;80(11):2087-2093.

31. Sanduleanu S, Jochems A, Upadhaya T, et al. Non-invasive imaging prediction of tumor hypoxia: a novel developed and externally validated CT and FDG-PET-based radiomic signatures. *Radiother Oncol*. 2020;153:97-105.

32. Mikhaeel NG, Heymans MW, Eertink JJ, et al. Proposed new dynamic prognostic index for diffuse large B-cell lymphoma: international metabolic prognostic index. *J Clin Oncol*. 2022;40(21):2352-2360.

33. Genta S, Ghilardi G, Cascione C, et al. Integration of baseline metabolic parameters and mutational profiles predicts long-term response to first-line therapy in DLBCL patients: a post hoc analysis of the SAKK38/07 study. *Cancers*. 2022;14(4):1018, 1-15.

34. Sha C, Barrans S, Cucco F, et al. Molecular high-grade B-cell lymphoma: defining a poor-risk group that requires different approaches to therapy. *J Clin Oncol*. 2019;37(3):202-212.

35. Lenz G, Wright G, Dave SS, et al. Stromal gene signatures in large-B-cell lymphomas. *N Engl J Med*. 2008;359(22):2313-2323.

36. Boellaard R, Delgado-Bolton R, Oyen WJG, et al. FDG PET/CT: EANM procedure guidelines for tumour imaging: version 2.0. *Eur J Nucl Med Mol Imag*. 2015;42(2):328-354.

37. Nioche C, Orhlac F, Boughdad S, et al. LIFEx: a freeware for radiomic feature calculation in multimodality imaging to accelerate advances in the characterization of tumor heterogeneity. *Cancer Res*. 2018;78(16):4786-4789.

38. Barrington SF, Meignan M. Time to prepare for risk adaptation in lymphoma by standardizing measurement of metabolic tumor burden. *J Nucl Med*. 2019;60(8):1096-1102.

39. Rizzo S, Botta F, Raimondi S, et al. Radiomics: the facts and the challenges of image analysis. *Eur Radiol Exp*. 2018;2(1):36, 1-8.

40. Kaplan EL, Meier P. Nonparametric estimations from incomplete observations. *J Am Stat Assoc*. 1958;53(282):457-481.

41. Hothorn T, Lausen B. Maximally selected rank statistics. *R News*. 2002;2:3-5.

42. *R Project*. Version 3.6.2. A language and environment for statistical computing. R Foundation for Statistical Computing; December 2019. http://www.R-project.org/

43. Derenzini E, Mazzara S, Melle F, et al. A 3-gene signature based on MYC, BCL-2 and NFKBIA improves risk stratification in diffuse large B-cell lymphoma. *Haematologica*. 2021;106(9):2405-2416.

44. Matassa DS, Amoroso MR, Lu H, et al. Oxidative metabolism drives inflammation-induced platinum resistance in human ovarian cancer. *Cell Death Differ*. 2016;23(9):1542-1554.

45. Evans KW, Yuca E, Scott SS, et al. Oxidative phosphorylation is a metabolic vulnerability in chemotherapy-resistant triple-negative breast cancer. *Cancer Res*. 2021;81(21):5572-5581.

46. McGuirk S, Audet-Delage Y, Annis MG, et al. Resistance to different anthracycline chemotherapeutics elicits distinct and actionable primary metabolic dependencies in breast cancer. *Elife*. 2021;10:e65150, 1-29.

47. Hlouschek J, Hansel C, Jendrossek V, Matschke J. The mitochondrial citrate carrier (slc25a1) sustains redox homeostasis and mitochondrial metabolism supporting radioresistance of cancer cells with tolerance to cycling severe hypoxia. *Front Oncol*. 2018;8:170, 1-18.

48. Woolbright BL, Choudhary D, Mikhalyuk A, et al. The role of pyruvate dehydrogenase kinase-4 (PDK4) in bladder cancer and chemoresistance. *Mol Cancer Therapeut*. 2018;17(9):2004-2012.

49. Zhao Z, Ji M, Wang Q, He N, Li Y. miR-16-5p/PDK4-mediated metabolic reprogramming is involved in chemoresistance of cervical cancer. *Mol Ther Oncolytics*. 2020;17:509-517.

50. Yu S, Li Y, Ren H, et al. PDK4 promotes tumorigenesis and cisplatin resistance in lung adenocarcinoma via transcriptional regulation of EPAS1. *Cancer Chemother Pharmacol*. 2021;87(2):207-215.

51. Mizutani H, Tada-Oikawa S, Hiraku Y, Kojima M, Kawanishi S. Mechanism of apoptosis induced by doxorubicin through the generation of hydrogen peroxide. *Life Sci*. 2005;76(13):1439-1453.

52. Mai Y, Yu JJ, Bartholdy B, et al. An oxidative stress-based mechanism of doxorubicin cytotoxicity suggests new therapeutic strategies in ABC-DLBCL. *Blood*. 2016;128(24):2797-2807.

53. Rossi A, Orecchioni S, Falvo P, et al. Dual targeting of the DNA damage response pathway and BCL-2 in diffuse large B-cell lymphoma. *Leukemia*. 2022;36(1):197-209.

54. Ravà M, D'Andrea A, Nicoli P, et al. Therapeutic synergy between tigecycline and venetoclax in a preclinical model of MYC/BCL2 double-hit B cell lymphoma. *Sci Transl Med*. 2018;10(426):1-9.

55. Lee D, Pagire HS, Pagire SH, et al. Discovery of novel pyruvate dehydrogenase kinase 4 inhibitors for potential oral treatment of metabolic diseases. *J Med Chem*. 2019;62(2):575-588.